Monthly Notices of the ROYAL ASTRONOMICAL SOCIETY

MNRAS **523,** 4923–4937 (2023) https://doi.org/10.1093/mnras/stad1703
Advance Access publication 2023 June 7

GRB 201015A and the nature of low-luminosity soft gamma-ray bursts

M. Patel [1]★ B. P. Gompertz [2] P. T. O'Brien,[1] G. P. Lamb [1,3] R. L. C. Starling [1] P. A Evans [1] L. Amati,[4] A. J. Levan,[5] M. Nicholl [2,6] K. Ackley,[7] M. J. Dyer [8] J. Lyman [7] K. Ulaczyk,[7] D. Steeghs [7] D. K. Galloway,[9,10,11] V. S. Dhillon [8,12] G. Ramsay,[13] K. Noysena,[14] R. Kotak,[15] R. P. Breton [16] L. K. Nuttall,[17] E. Pallé[12] and D. Pollacco[7]

[1]*School of Physics and Astronomy, University of Leicester, University Road, Leicester LE1 7RH, UK*
[2]*School of Physics and Astronomy & Institute for Gravitational Wave Astronomy, University of Birmingham, Birmingham B15 2TT, UK*
[3]*Astrophysics Research Institute, Liverpool John Moores University, IC2 Liverpool Science Park, 165 Brownlow Hill, Liverpool L3 5RF, UK*
[4]*INAF – IASF Bologna, via P. Gobetti 101, Bologna, Italy*
[5]*Department of Astrophysics/IMAPP, Radboud University, P.O. Box 9010, NL-6500 GL Nijmegen, the Netherlands*
[6]*Astrophysics Research Centre, School of Mathematics and Physics, Queen's University Belfast, Belfast BT7 1NN, UK*
[7]*Department of Physics, Warwick University, Coventry CV4 7AL, UK*
[8]*Department of Physics and Astronomy, University of Sheffield, Sheffield S3 7RH, UK*
[9]*School of Physics & Astronomy, Monash University, Wellington Rd, Clayton, VIC 3800, Australia*
[10]*OzGRav-Monash, School of Physics & Astronomy, Monash University, Clayton, VIC 3800, Australia*
[11]*Institute for Globally Distributed Open Research and Education (IGDORE), Box 1074, Kristinehöjdsgatan 9A, Gothenburg, SE-412 82, Sweden*
[12]*Instituto de Astrofisica de Canarias, E-38205 La Laguna, Tenerife, Spain*
[13]*Armagh Observatory & Planetarium, College Hill, Armagh BT61 9DB, UK*
[14]*National Astronomical Research Institute of Thailand, Don Kaeo, Mae Rim District, Chiang Mai 50180, Thailand*
[15]*Department of Physics and Astronomy, University of Turku, FI-20500 Turku, Finland*
[16]*Department of Physics and Astronomy, University of Manchester, Oxford Rd, Manchester M13 9PL, UK*
[17]*School of Mathematics & Physics, University of Portsmouth, University House, Winston Churchill Ave, Portsmouth PO1 2UP, UK*

Accepted 2023 May 27. Received 2023 May 23; in original form 2023 February 20

ABSTRACT

GRB 201015A is a peculiarly low luminosity, spectrally soft gamma-ray burst (GRB), with $T_{90} = 9.8 \pm 3.5$ s (time interval of detection of 90 per cent of photons from the GRB), and an associated supernova (likely to be type Ic or Ic-BL). GRB 201015A has an isotropic energy $E_{\gamma,\rm iso} = 1.75^{+0.60}_{-0.53} \times 10^{50}$ erg, and photon index $\Gamma = 3.00^{+0.50}_{-0.42}$ (15–150 keV). It follows the Amati relation, a correlation between $E_{\gamma,\rm iso}$ and spectral peak energy $E_{\rm p}$ followed by long GRBs. It appears exceptionally soft based on Γ, the hardness ratio of HR $= 0.47 \pm 0.24$, and low-$E_{\rm p}$, so we have compared it to other GRBs sharing these properties. These events can be explained by shock breakout, poorly collimated jets, and off-axis viewing. Follow-up observations of the afterglow taken in the X-ray, optical, and radio reveal a surprisingly late flattening in the X-ray from $t = (2.61 \pm 1.27) \times 10^4$ s to $t = 1.67^{+1.14}_{-0.65} \times 10^6$ s. We fit the data to closure relations describing the synchrotron emission, finding the electron spectral index to be $p = 2.42^{+0.44}_{-0.30}$ and evidence of late-time energy injection with coefficient $q = 0.24^{+0.24}_{-0.18}$. The jet half opening angle lower limit ($\theta_{\rm j} \geq 16^\circ$) is inferred from the non-detection of a jet break. The launch of SVOM and Einstein Probe in 2023 should enable detection of more low-luminosity events like this, providing a fuller picture of the variety of GRBs.

Key words: gamma-ray burst: general – gamma-ray burst: individual: GRB 201015A – gamma-ray bursts – transients: supernova.

1 INTRODUCTION

Several thousand gamma-ray bursts (GRBs) have been detected since their first identification more than 50 years ago Klebesadel, Strong & Olson (1973). These bursts of gamma-rays are detected by satellites such as the *Neil Gehrels Swift Observatory* (Gehrels et al. 2004) or *Fermi* (Meegan et al. 2009). For the majority of these events, information is only available in the γ −ray bands, typically in the range from tens of keV to a few MeV, providing both temporal and spectral information (Piran 2005). On the basis of these data alone the population is highly varied, but the duration of the bursts is clearly bimodal, splitting the long and short GRBs at a boundary at $T_{90} \sim 2$ s (Kouveliotou et al. 1993), where T_{90} is the duration in which 90 per cent of the photons from the GRB are detected (Koshut et al. 1995). The short GRB population typically has harder spectra, meaning there is a larger proportion of higher energy photons to lower-energy photons, compared to long GRBs (Zhang, Lü & Liang 2016).

Intensive multiwavelength observations of GRBs over the past 30 years have revealed that these two populations arise from distinct progenitors (e.g. Chevalier & Li 1999; Levan et al. 2016). The long

★ E-mail: mp664@leicester.ac.uk

GRBs (LGRBs), lasting typically from a few seconds up to several minutes or longer, arise from star-forming galaxies (Fruchter et al. 2006), and photometric and spectroscopic monitoring has revealed that they are created in the core-collapse of massive, rapidly spinning, likely low-metallicity stars creating a supernova type I b/c counterpart to the GRB (Hjorth et al. 2003; Stanek et al. 2003; Levan 2018). This event is also referred to as a collapsar. The first evidence of this origin of long GRBs came from the direct association of GRB980425 with SN1998bw, a peculiar type Ib/c SN (Galama et al. 1999).

In contrast, the short GRBs (SGRBs), lasting from few hundreds of ms up to 2 s (Kouveliotou et al. 1993), are found in galaxies of all ages, sometimes at large distances from their hosts (Fong et al. 2022). The identification of possible kilonovae (Tanvir et al. 2013; Troja et al. 2017; Lamb et al. 2019), powered by radioactive decays of r-process elements, and ultimately the near-simultaneous detection of a short GRB with the gravitational wave detected merger GW170817 secured their origin in the mergers of compact objects (Abbott et al. 2017). Although, short GRBs are almost always viewed on-axis, GRB 170817A was viewed at ≤ 36 degrees from the jet axis (Abbott et al. 2017), and GRB 150101B, was significantly under-luminous and later shown to be viewed off-axis by 13 degrees (Troja et al. 2018).

For both the collapsar or compact object merger scenarios, the central engine (an accreting black hole or neutron star) launches relativistic jets of material (e.g. Kluźniak & Ruderman 1998; Lei, Zhang & Liang 2013; Lü et al. 2015). Gamma-rays are produced via either self-interactions of this material (Sari, Piran & Halpern 1999; Mészáros 2002) or the dissipation of magnetic fields (Beniamini & van der Horst 2017). As the jets plough into the circumstellar environment they are decelerated and shock fronts interact with the surrounding material, forming a broad-band synchrotron 'afterglow' (Gao et al. 2013b; Iyyani et al. 2016).

There are suggestions of additional categorizations of GRBs, for example a separate 'intermediate' duration population lasting 2–5 s (e.g. Mukherjee et al. 1998; Tunnicliffe & Levan 2012), low-luminosity GRBs with luminosity $L < 10^{49}$ erg s^{-1} (Liang et al. 2007; Virgili, Liang & Zhang 2008), or events which are 'ultra-long' (Levan et al. 2014). However, the reality of these populations, and if they represent distinct physical processes remains unclear. We recognize that there is a lot of variation within the GRB population. They range in duration from milliseconds to hours, have spectral peaks ranging from the keV to MeV range, and isotropic energies ranging from 10^{46} to 10^{54} erg (Virgili et al. 2008; Levan et al. 2016). Some have very smooth light curves, others demonstrate pronounced variability (Zhang et al. 2016). It is therefore quite plausible that additional mechanisms are present within the observed populations (Nousek et al. 2006).

Indeed, it is striking that there are a small number of apparently long GRBs which do not exhibit supernova signatures, which are suggested to arise from mergers such as GRB211211A, which has an observed kilonova counterpart (Rastinejad et al. 2022). These SGRBs are detected as long GRBs based on their T_{90} in the γ-ray band, but have multiple spikes with extended emission (EE-SGRBs) (e.g. Gehrels et al. 2006; Zhang et al. 2020a; Gompertz et al. 2023). There are also discoveries of short-duration GRBs with a core-collapse supernova association (e.g. Ahumada et al. 2021; Amati 2021; Zhang et al. 2021). A re-analysis of the prompt GRB emission properties using a machine learning based approach is largely successful at splitting GRBs into the two merger and collapsar groups, however, some GRBs are incorrectly classified, and some fail to be robustly classified (Jespersen et al. 2020).

To understand the nature of GRBs therefore continues to require further observations, in particular of bursts which appear to defy ready classification within a single scheme, for example long-GRBs without associated supernovae or in older galaxies; GRBs which appear under- or overluminous, or bursts which touch on the extremes of duration, spectrum, variability or other key indicators.

Here we consider the case of GRB 201015A, a GRB close to the long-short GRB divide, exhibiting a short peak and extended emission morphology in the prompt emission light curve (Markwardt et al. 2020). Strikingly, it was also extremely spectrally soft, much softer than the majority of short, or even long-GRBs (Lien et al. 2016). The detection of a supernova confirms this GRB to have a collapsar progenitor (Rossi et al. 2021).

This GRB has been of interest due to the possible very high energy (VHE) detection at TeV energies (Blanch et al. 2020). The MAGIC collaboration reported a 3.5σ detection of the GRB 201015A in TeV energies beginning 33s after the trigger (Suda et al. 2021). This makes GRB 201015A the fifth burst to be detected in very high energy (VHE), giving possible further evidence of Synchrotron self-Compton (SSC) emission (Nava 2018). This is the process of Synchrotron photons – produced from electrons accelerated in a magnetic field – scattering off electrons making them more energetic. The other GRBs detected in VHE by the MAGIC and H.E.S.S. collaborations are GRB 190114C, GRB 180720B, GRB 190829A, and GRB 201216C. This sample already includes a variety of both high and low prompt energy GRBs with GRB 190114C having $E_{\gamma,\mathrm{iso}}=3 \times 10^{53}$ erg and GRB 190829A having $E_{\gamma,\mathrm{iso}}=2 \times 10^{50}$ erg (Berti & Carosi 2022). GRB 201015A adds another low-luminosity GRB to the sample.

The afterglow observations in radio by the VLBI telescope as well as afterglow measurements in other wavebands have been studied. Giarratana et al. (2022) compares the GRB 201015A to other VHE bursts, and uses afterglow models to suggest this is an on-axis GRB expanding into a homogeneous ISM-like medium. In this paper, we look into the initial energetics of the burst, comparing the isotropic energy, $E_{\gamma,\mathrm{iso}}$, and spectral peak energy E_{p}, to the Amati relation for long GRBs (Amati 2006). We identify and compare a sample of similar bursts in terms of the soft prompt spectrum and low luminosity and low Epeak. We have also collated multiwavelength information on the afterglow of GRB 201015A and related this to models to explain an observed break in the X-ray afterglow.

In Section 2, we present the data we have collected of the prompt and afterglow emission of GRB 201015A, and Section 3 goes through the fitting of models to the afterglow and SN, as well as predicting the duration of the X-ray plateau, and minimum jet opening angle. We then compare GRB 201015A to other spectrally soft GRBs in Section 4, and discuss our findings in Section 5, and provide conclusions in Section 6. The optical data is fairly extensive, so it is presented in the Appendices. The findings presented in this paper are quoted with 1σ confidence regions. A flat ΛCDM cosmology with $\Omega_{\mathrm{m}} = 0.3$, $\Omega_{\Lambda} = 0.7$, $H_0 = 65$ km s^{-1} Mpc^{-1} has been assumed for this work. In this paper, we define the spectral index, β, as $F(\nu)_{\nu} \propto \nu^{-\beta}$ and similarly for the temporal power-law relation $F(\nu)_{\mathrm{t}} \propto t^{-\alpha}$. The equation describing the relation between the photon index, Γ, and spectral index, β, is: $\Gamma = \beta + 1$.

2 OBSERVATIONS

2.1 Discovery of GRB 201015A

Here we present the observations detailed in the public Gamma-ray Burst Coordinates Network (GCN). The *Swift* Burst Alert Telescope

(BAT; Barthelmy et al. 2005) triggered on GRB 201015A at 22:50:13 UT (hereafter T_0) (D'Elia et al. 2020). The refined BAT analysis reveals the position of this source to be RA = 354.342, DEC = 53.393 (Markwardt et al. 2020). The BAT light curve shows a short initial spike of overlapping pulses that lasts for ∼1s, followed by a tail of extended emission that lasts until ∼10s, exhibiting a similar morphology to EE-GRBs (Norris, Gehrels & Scargle 2010). The prompt emission in the 15–350 keV range has a duration of $T_{90} = 9.78 \pm 3.47$s (Markwardt et al. 2020). The time-averaged BAT spectrum (from $T + 0.02$ to $T + 10.35$ s) is best fit by a power-law model with a photon index of $\Gamma = 3.03 \pm 0.68$ (Markwardt et al. 2020).

The *Fermi* Gamma-ray Burst Monitor (GBM; Meegan et al. 2009) detected a weak, subthreshold event with a duration of ∼1s (Fletcher, Veres & Fermi-GBM Team 2020). The spectrum is adequately fit by a Band function (Band et al. 1993) with a peak energy of $E_{\rm p} = 14 \pm 6$ keV, a fixed low-energy index of $\beta_1 = 1$, and a high-energy index of $\beta_2 = 2.40 \pm 0.21$. This model yields a 10–1000 keV fluence of $(2.25 \pm 0.38) \times 10^{-7}$ erg cm^{-2} (Fletcher et al. 2020), resulting in $E_{\gamma,\rm iso} = (1.1 \pm 0.2) \times 10^{50}$ erg. Due to an observing constraint, *Swift* was unable to slew to GRB 201015A until $T_0 + 51.6$ min. Once on target, the X-ray Telescope (XRT; Burrows et al. 2005) detected a fading, uncatalogued X-ray source within the BAT error circle. The combined XRT-UVOT observations reveal a source at RA(J2000) = 23:37:16.43, Dec(J2000) = + 53:24:57.5 with an uncertainty of 1.9 arcsec (radius, 90 per cent containment) (Goad et al. 2007; Evans et al. 2009, 2020). The XRT (0.3–10 keV) afterglow light curve, between 0.03 and 21 d after the trigger, decays with a power-law index of $\alpha_x = 1.80^{+0.22}_{-0.20}$, according to the live XRT GRB catalogue.[1] (Evans et al. 2009).

The MAGIC telescope's 3.5σ detection of the source came from almost 4 h of observation starting at $T_0 + 33s$ finding evidence of $>140GeV$ emission from GRB 201015A (Suda et al. 2021).

An optical transient coincident with the BAT error circle was first reported by MASTER (Lipunov et al. 2010) 88s after the trigger (Lipunov et al. 2020) and prior to the XRT detections. This was confirmed to be the afterglow by the Nordic Optical Telescope (NOT; Malesani, de Ugarte Postigo & Pursimo 2020) and the Gravitational-wave Optical Transient Observer (GOTO; Ackley et al. 2020). An uncatalogued host galaxy with magnitude $r = 22.9 \pm 0.2$ was identified coincident with the GRB position, separated by 2.3' (Rastinejad et al. 2020; Rossi et al. 2021). Optical observations by GTC/OSIRIS started at $T_0 + 5.28$ h providing a spectrum from 3700 to 7800 Å. A redshift of $z = 0.426$ was calculated from [OIII], [OII], and H-β emission lines identified above the continuum (de Ugarte Postigo et al. 2020).

Radio observations were taken by the VLA at a central frequency of 6 GHz 1.41 d after the trigger showing a flux density of ∼0.13 mJy (Fong et al. 2020). Following this the e-Merlin telescope observed the transient at a central frequency of 1.5 GHz at 19 and 23 d after the trigger. The measured flux densities were $(2.14 \pm 0.25) \times 10^{-4}$ Jy and $(2.56 \pm 0.27) \times 10^{-4}$ Jy respectively (Rhodes et al. 2020). Both sources were found to be at a consistent position with the optical afterglow.

2.2 Gamma-rays

We downloaded the BAT spectral files from the *Swift*/BAT catalogue (Lien et al. 2016) to perform an independent analysis using XSPEC v12.11.1. The time-averaged total BAT spectrum is referred to as the BAT T_{100} in this paper. We fit a singe power-law to the BAT T_{100} spectrum with duration 10.32 s in the 15–150 keV energy bands using XSPEC, fitting with chi-squared statistics. The result is a photon index of $\Gamma = 3.00^{+0.50}_{-0.42}$ with normalization $K = 200^{+744}_{-200}$ photons keV^{-1} cm^{-2} s^{-1} at 1 keV. The fit has a reduced chi-squared value of $\chi^2_\nu = 1.03$ with 56 degrees of freedom. The measured photon index is unusually soft, particularly in the BAT band. Lien et al. (2016) showed that the photon indices measured for single power-law fits to BAT data of SGRBs are distributed around $\Gamma \approx 1.5 \pm 0.5$, and for LGRBs around $\Gamma \approx 2.0 \pm 0.5$. In fact, only three other GRBs in the sample of Lien et al. (2016) have measured photon indices $\Gamma > 3$ with constrained confidence regions. These GRBs are: 050416A, 080 520 and 140622A, and we have analysed them in this paper.

Table 1. Table of spectral model parameters resulting from XSPEC fitting of BAT spectra of GRB 201015A.

Spectrum	Model	Parameters	χ^2_ν
BAT	Power law	$\Gamma = 3.00^{+0.50}_{-0.42}$	1.03
T_{100}		$K = 200^{+744}_{-200}$ cts keV^{-1} cm^{-2} s^{-1}	

In order to compare the energetics of GRB 201015A to other GRBs, we calculate the spectral peak energy, $E_{\rm peak}$, and isotropic equivalent energy, $E_{\gamma,\rm iso}$. The time-averaged BAT spectrum (with exposure time $T_{100} = 10.32s$) in the 15–150 keV band was used to fit both a cut-off power-law (CUTOFFPL) and Band function (GRBM) (Band et al. 1993) using XSPEC to determine the spectral peak. For these two spectral models, it was difficult to constrain the 1σ confidence region on some of the parameters including the spectral break. Using an f-test to determine the best fit we found that the simple power-law described above provided a better fit for this GRB than a model with additional parameters.

A summary of the fitting can be found in the Table 1. After finding a suitable fit, the normalization parameter was frozen, and the CFLUX component was added to the model to determine the flux.

The intrinsic spectral peak energy is calculated using the characteristic energy E_0, power-law index β, and redshift z, with the following formula.

$$E_{\rm peak,i} = E_0(2 - \beta)(1 + z) \quad (1)$$

For this GRB, however, we have not observed the spectral peak energy, so it is assumed to be below the lower-limit of the detector bandpass (15 keV), which is consistent with the result of 14 ± 6 keV from the Band function fit to the *Fermi* spectrum (Fletcher et al. 2020). Correcting for redshift results in $E_{\rm peak,\,i} < 21.39$ keV.

The isotropic equivalent energy of the burst was calculated using:

$$E_{\gamma,\rm iso} = F_{\rm d} T_{100} \frac{F_{\rm iso}}{F_{\rm d}} \frac{4\pi D_{\rm L}}{1+z} \quad (2)$$

where $F_{\rm d}$ is the flux in the detector energy band, $F_{\rm iso}$ is the flux in 10–10,000 keV in the rest frame of the GRB, T_{100} is the duration of the burst, $D_{\rm L}$ is the luminosity distance, z is the redshift. We find that $E_{\gamma,\rm iso} = 1.75^{+0.60}_{-0.53} \times 10^{50}$ erg for this burst. This is a low $E_{\gamma,\rm iso}$ value for a GRB considering most GRBs fall in the range of 10^{52-54} erg (Levan et al. 2016). The $E_{\rm p}$ value is also lower than most GRBs which have a typical $E_{\rm p} \sim 250$ keV (Soderberg et al. 2004). Previously, events with $E_{\rm p} < 30$ keV were classified as X-ray flares (XRF) (Zhang et al. 2020c).

[1] https://www.swift.ac.uk/xrt_live_cat/01000452/

Table 2. Table of spectral model parameters resulting from XSPEC fitting of the XRT time-averaged spectrum of GRB 201015A.

Spectrum	Model	Parameters	C-stat	Degrees of freedom
XRT	power law × TBABS × ZTBABS	$\Gamma = 2.16^{+0.24}_{-0.23}$	132.85	132
$T_0 + (3217 - 22019)s$		$n_{\rm H} = 3.6 \times 10^{21}$		
		$z = 0.426$		
		$n_{{\rm H},z} = (2.1^{+2.4}_{-1.9}) \times 10^{21}$		
		$K = (5.7^{+1.6}_{-1.2}) \times 10^{-4}$ photons keV^{-1} cm^{-2} s^{-1}		

Table 3. X-ray observations of GRB 201015A with *Swift*-XRT and *Chandra*-ACIS.

Mean time since trigger (s)	Exposure (s)	Flux density at 1 keV (μJy)	Telescope
3315.92	167.99	1.42 ± 0.31	XRT
3478.46	193.06	1.18 ± 0.27	XRT
3695.51	250.73	0.90 ± 0.20	XRT
3995.15	335.97	1.01 ± 0.19	XRT
4529.49	271.96	0.78 ± 0.21	XRT
4758.91	300.88	0.78 ± 0.17	XRT
9997.85	260.76	0.66 ± 0.17	XRT
10627.34	882.58	0.19 ± 0.05	XRT
13568.17	11036.42	0.14 ± 0.03	XRT
56362.31	1795.23	$(3.45^{+1.94}_{-1.43}) \times 10^{-2}$	XRT
66939.88	1384.03	<0.12	XRT
725760.00	28800.00	$(1.56 \pm 0.07) \times 10^{-2}$	ACIS
1179360.00	43200.00	$(1.36 \pm 0.05) \times 10^{-2}$	ACIS
1760376.71	322497.18	$(8.48^{+3.27}_{-2.72}) \times 10^{-3}$	XRT

2.3 X-rays

The early time-averaged XRT spectrum ($T_0 + 3217$ to 22 019 s) produced by the *Swift* Burst Analyser[2] (Evans et al. 2010) using HEASoft v6.29 is well fitted within XSPEC (Arnaud 1996). We used a composite model comprised of a power-law × TBABS (Wilms, Allen & McCray 2000) × ZTBABS. This yields a photon index of $\Gamma = 2.16^{+0.24}_{-0.23}$ and an intrinsic absorption column of $n_{H,z} = (2.1^{+2.4}_{-1.9}) \times 10^{21}$ cm^{-2} at the redshift of the GRB ($z = 0.426$), with normalization $(5.7^{+1.6}_{-1.2}) \times 10^{-4}$ photons keV^{-1} cm^{-2} s^{-1} at 1 keV (C-stat = 132.85 for 132 degrees of freedom). Fitting was performed using Cash statistics (Cash 1979), and the Galactic absorption column was fixed to $n_{\rm H} = 3.60 \times 10^{21}$ cm^{-2} (Willingale et al. 2013). We added a blackbody component to the model to check for thermal emission, but this model did not provide a fit as good as the simple power-law with absorption. The results of the best spectral fit are provided in Table 2.

We triggered target of opportunity (ToO) observations with the *Chandra* X-ray Observatory under proposal ID 22 400 511 (PI: Gompertz). We obtained two epochs of observations with the ACIS-S instrument in Very Faint (VF) mode on the 24$^{\rm th}$ and 29$^{\rm th}$ of October. The exposure times were 35 ks and 45 ks, respectively. The afterglow is clearly detected in both epochs, with 0.5–7 keV count rates of $(4.07 \pm 0.38) \times 10^{-3}$ cts s^{-1} 8.4 d after trigger and $(3.11 \pm 0.29) \times 10^{-3}$ cts s^{-1} 13.6 d after trigger.

Data were analysed using XSPEC V12.11.1. In order to account for the possibility of a spectral change during the large gap in coverage between the early XRT data and our first *Chandra* observation, we performed a simultaneous spectral fit of the two *Chandra* epochs and the late *Swift* epoch. This is the same data processing method as used in Giarratana et al. (2022). The simultaneous spectral model is the same as for the early XRT data (i.e. power-law × TBABS × ZTBABS), with absorption fixed to the previous values. Our best fit is $\Gamma = 2.10 \pm 0.13$, indicating that the spectrum has not changed significantly.

The full X-ray light curve is shown in Table 3. XRT data have been absorption corrected using the ratio of counts-to-flux unabsorbed over counts-to-flux observed reported in the time-averaged spectral fit on the UKSSDC. For the *Chandra* data, we extract the unabsorbed 0.3–10 keV fluxes using the XSPEC routine CFLUX and the model fit described previously. Fluxes are then converted to flux densities using (cf. Gehrels et al. 2008)

$$F_{\nu,x} = 4.13 \times 10^{11} \frac{F_x (2-\Gamma) E_0^{1-\Gamma}}{E_2^{2-\Gamma} - E_1^{2-\Gamma}} \ \mu{\rm Jy}. \quad (3)$$

E_0 is the flux density energy (we set 1 keV). E_1 and E_2 are the lower and upper bounds of the flux bandpass, respectively.

The resulting light curve is well fit ($\chi^2_\nu = 0.78$ with 10 degrees of freedom) with a broken power-law model with indices $\alpha_1 = 1.53 \pm 0.14$ and $\alpha_2 = 0.48 \pm 0.12$ either side of a break at $t_{\rm b} = (2.61 \pm 1.27) \times 10^4$s (Fig. 1). This differs from the fitting of the X-ray data in Giarratana et al. (2022) where this data was approximated to a simple power-law. The broken-power law model for the X-ray afterglow implying a plateau phase affects the closure relation model which describes the synchrotron emission being observed. This long-lasting plateau at late-time is unexpected since it is ongoing until at least $\sim 10^6$ s, as Tang et al. (2019) found the plateau end time falls between $(0.9 - 10) \times 10^3$s for 50 per cent of GRBs with a plateau in the X-ray. We consider the causes for this plateau in Section 3.1 by analysing the closure relations that best fit this afterglow.

2.4 Optical

The GOTO telescope Steeghs et al. (2022) began observations of the target 51 mins after the trigger with 4 × 90s exposures using the wide L-band filter (400-700 nm). The source was identified and photometrically calibrated in the following manner. A first pass at source detection is made using SExtractor (Bertin & Arnouts 1996) to identify source positions and preliminary instrumental magnitudes. From the catalog positions, an initial astrometric solution is generated using ASTROMETRY.NET (Lang et al. 2010). This solution is further refined if necessary by cross-matching the solved positions against the ATLAS-REFCAT2 (Tonry et al. 2018) astrometric catalog. Any further refinements to the SIP (Simple Imaging Polynomial) distortion parameters of the WCS (World Coordinate System) solution is completed using a custom package[3] Using cross-calibration against the same ATLAS-REFCAT2 catalog and using magnitude zeropoints calibrated against the AAVSO Photometric

[2] https://www.swift.ac.uk/burst_analyser/

[3] https://github.com/GOTO-OBS/goto-astromtools

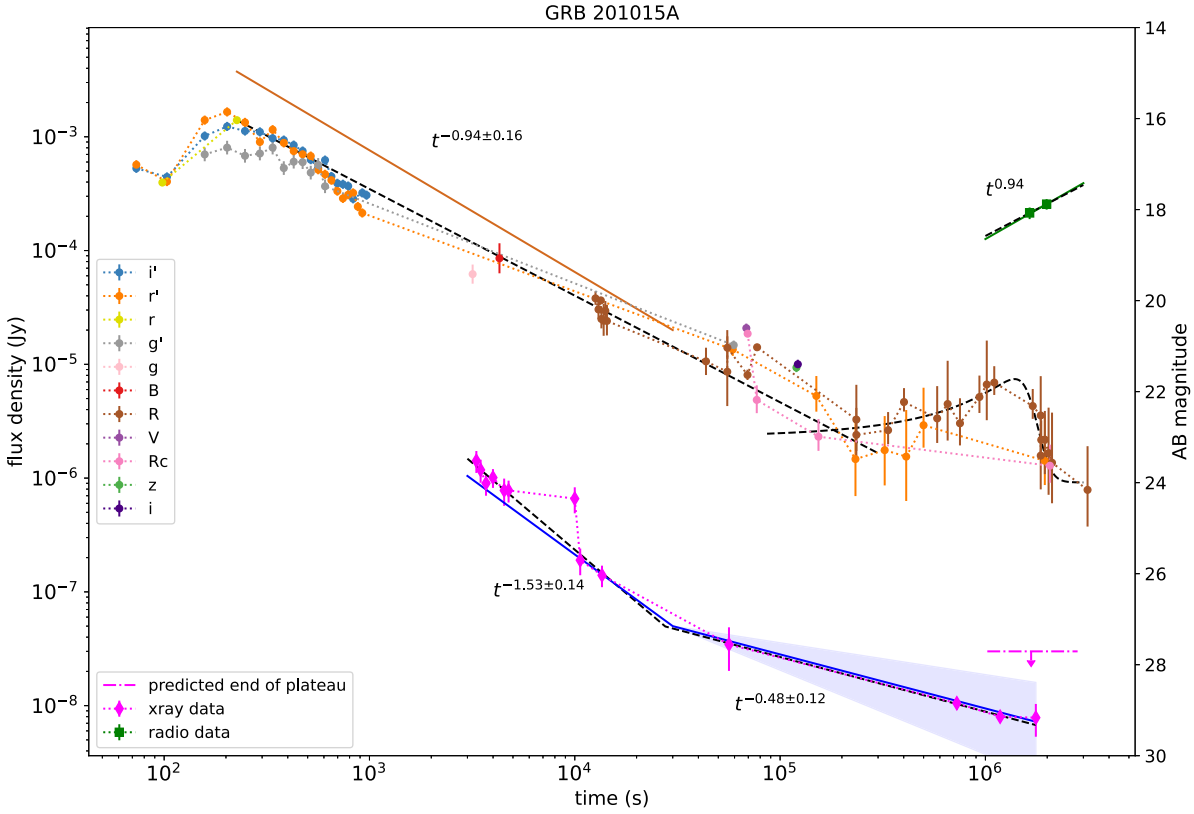

Figure 1. A plot of the afterglow observational data (dotted lines) of the GRB 201015A with the best-fitting power laws and supernova model (black dashed lines) and closure relation (solid coloured lines; Gao et al. 2013a). The optical afterglow of GRB 201015A is found from data published in GCNs, showing a mean power-law decay constant of -0.94 ± 0.16 after the peak at 226 ± 26 s. The X-ray data from *Swift* XRT and *Chandra* is fitted to a broken power law with the decay constants -1.53 ± 0.14 and -0.48 ± 0.12 with a break at 26 ks. Radio data collected by e-MERLIN, also taken from GCNs, give a decay constant of $\sim$0.94. The closure relations are plotted with the mean value of the electron spectral index $p = 2.42^{+0.44}_{-0.30}$, and the blue shaded region represents the upper and lower decay constants from the lower and upper confidence regions of the energy injection coefficient $q = 0.24^{+0.24}_{-0.18}$. The pink arrow represents the prediction, based on the Dainotti relation, for the end time of the plateau phase of the afterglow with the dash-dotted line expanding to the 1σ lower and upper confidence regions (Dainotti et al. 2015).

All-Sky Survey (APASS) survey[4], an equivalent APASS g'-band magnitude of the optical afterglow was found to be $g = 20.54 \pm 0.21$. We triggered target of opportunity (ToO) observations with the Liverpool Telescope (LT; Steele et al. 2004) under program PL20B21 (PI: Gompertz). We obtained four epochs of observations with the IO:O instrument using the r' and i' filters (Fukugita et al. 1996), beginning on the night of the 16th of October ($\sim$1 day after trigger). The individual images are aligned using SPALIPY[5] and stacked. Photometry is performed with SEP[6] (Bertin & Arnouts 1996; Barbary 2016). Magnitudes are extracted with a 3 pixel aperture radius, which minimizes the confidence interval while avoiding unwanted light from the complicated field. Photometric zero points were computed using nearby field stars in the Pan-STARRS catalog (Chambers et al. 2016).

The optical data collected from all the GCNs is shown in the Appendices. These data were then corrected for extinction based on the position of the afterglow and the waveband of the observation using the IRSA Galactic Dust Reddening and Extinction tool[7] The magnitudes from the various filters were converted to AB magnitudes and flux density (Jy) using the zero points from Frei & Gunn (1994).

We fit a broken power-law to the afterglow light curve up to 3×10^5 s. We find that the peak is at $t_d = 226 \pm 26$ s which is the deceleration time. After the peak, the power-law decays at $\alpha = 0.94 \pm 0.16$. The data after 1 day are fit to the analytic supernova model from (Bazin et al. 2011) described in Section 3.2.

Limited spectral information was available from this data, but we used the simultaneous observations in g', r', and i' bands by the NUTTela-TAO Burst Simultaneous Three-Channel Imager (BSTI) instrument, to infer the spectral index over the time period $\sim$150 − 600 s. We fit a power-law to the extinction corrected magnitudes against central wavelength of the filters for each epoch with multiple filter observations. We then calculate the average spectral index with weighting of $1 - (\sigma/\mathrm{sum}(\sigma))$ resulting in average spectral index of 0.75 ± 0.39 in the early optical data. 440.0pt

2.5 Radio

In Table 4, we have tabulated the radio (1.5 GHz) observations by e-Merlin taken on 3rd and 7th November 2020 presented in the GCN notices (Rhodes et al. 2020). We fit a simple power-law to the flux densities to determine the decay of the radio light curve: $\alpha \sim -0.94$.

[4] http://www.aavso.org/apass
[5] https://pypi.org/project/spalipy/
[6] https://sep.readthedocs.io/en/v1.0.x/index.html
[7] https://irsa.ipac.caltech.edu/applications/DUST/

Table 4. Tabulated values of the radio observations of GRB 201015A reported in Rhodes et al. (2020).

Time (s)	Flux density (Jy)	Frequency	Telescope
1.642×10^6	$(2.14 \pm 0.25) \times 10^4$	1.5×10^9	e-Merlin
1.987×10^6	$(2.56 \pm 0.27) \times 10^4$	1.5×10^9	e-Merlin

Suitable errors could not be provided for this fit due to the lack of observations.

3 ANALYSIS

3.1 Closure relations

The relations between the spectral index β and the temporal index α based on the synchrotron external shock model, are termed the closure relations (Sari, Piran & Narayan 1998; Zhang & Mészáros 2004). As the GRB ejecta jet propagates forward, it collides with the circumburst medium creating forward and reverse shock waves, resulting in further shocks. This relation arises from the synchrotron radiation emitted by the accelerated electrons in the magnetic field. The afterglow is described as $F_\nu \propto \nu^{-\beta} t^{-\alpha}$ The electron spectral index p determines the parameters of the closure relation.

We use the temporal and spectral indices described in Section 2, which are summarized below and in Table 5, to compare the observational data to the theoretical framework. The X-ray light curve is best described by a broken power-law with $\alpha_{x1} = 1.53 \pm 0.14$ and $\alpha_{x2} = 0.48 \pm 0.12$. The break indicating the start of the plateau phase is at $t_b = (2.61 \pm 1.27) \times 10^4$ s. The spectral index of the first phase is $\beta_{x1} = 1.16 \pm 0.22$, and $\beta_{x2} = 1.10 \pm 0.13$ for the second phase. The optical light curve after the peak at $t_d = 226 \pm 26$ s has a decay of $\alpha_o = 0.94 \pm 0.16$ and the spectral index is measured to be $\beta_o = 0.75 \pm 0.38$ from $\sim 150 - 600$ s. We could not get spectral information after the t_b time because there were no simultaneous observations with different filters as provided by the NUTTelA-TAO BSTI for the early time data. The temporal index after the break could not be determined due to the supernova. The radio provides late time information in a different waveband after t_b demonstrating a temporal index of $\alpha_r \approx -0.94$. The light curve is shown in Fig. 1. The closure relations (CR) can provide a diagnostic for the surprising late-time rebrightening in the X-ray.

To find the electron spectral index p, we calculated it independently using the α and β values for the optical and X-ray observations before the break time t_b, and found the average for the scenario where the results are consistent with each other. We considered the wind to ISM transition as a possible explanation for the steep-to-shallow transition such as the case with GRB 140423A (Li et al. 2020). However this failed to converge in consistent values of p. The best case scenario was relativistic, isotropic, self-similar deceleration phase for $\nu_a < \nu_m < \nu_c$ in ISM, in the slow cooling regime, with $p = 2.42^{+0.44}_{-0.30}$.

To explain the afterglow after the break, we needed to introduce energy injection. The shallowing of the light curve can be explained by the process of continuous energy injection from the central engine, possibly an accreting supra-massive neutron star, or magnetar or black hole (Chen et al. 2017; Li et al. 2018). The luminosity of this central engine is given by (Zhang & Mészáros 2001)

$$L = L_0 \left(\frac{t}{t_0}\right)^{-q} \tag{4}$$

where t_0 is the time at which the self-similar solution forms and the external shocks begin to decelerate, and q is the energy injection parameter (Zhang & Mészáros 2001; Li et al. 2018). Evidence of the injection would be present in the afterglow when $q < 1$. Values of $q \sim 0.3$ are typical for GRBs expected to have energy injection from a magnetar or black hole (Li et al. 2018). Another possibility is the energy injection from slower shells of ejecta catching up to the initial decelerating shock wave (Zhang et al. 2006). In this scenario, the energy injection is described as $E_{iso} \propto \gamma^{1-s}$ where γ is the Lorentz factor, and s is the shell model energy injection parameter. We calculated the value of q from the energy injection equation in Gao et al. (2013a):

$$\alpha = \frac{(2p-4) + (p+2)q}{4} \tag{5}$$

using the measured value of $\alpha_{x,2}$ and the value of p found above. The shallowing of the light-curve in the X-ray can be explained by energy injection parameter $q = 0.24^{+0.24}_{-0.18}$. The 1σ confidence range of q relates to $\alpha_{x,2} = 0.48^{+0.26}_{-0.20}$. This range is denoted by the blue shaded region in Fig. 1 along with the slopes for each of the light curves from the CR. The spectral and temporal indices given by the described CR are given in Table 5.

3.2 Supernova

The optical observations later than 1 day show evidence of a supernova. The following analytic supernova model used in Taddia et al. (2015) and Bazin et al. (2011) was fit to the data:

$$F(t) = A \frac{e^{\left(-\frac{t-t_0}{\tau_{fall}}\right)}}{1 + e^{\left(-\frac{t-t_0}{\tau_{rise}}\right)}} + c \tag{6}$$

where $F(t)$ is the flux density, t is the time, A and c are normalization constants, and t_0, τ_{fall} and τ_{rise} are related to the time of the peak of the supernova:

$$t_{peak} = t_0 + \tau_{rise} \ln\left(\frac{\tau_{fall}}{\tau_{rise}} - 1\right) \tag{7}$$

Table 5. The spectral and temporal indices in the best-fitting closure relation for this afterglow (relativistic, isotropic, self-similar deceleration phase for $\nu_a < \nu_m < \nu_c$ in ISM, with $p = 2.42^{+0.44}_{-0.30}$), compared with the measured values for the relevant frequency ranges, both before and after energy injection at $\sim 3 \times 10^4$ s with $q = 0.24^{+0.24}_{-0.18}$.

		Temporal index α		Spectral index β	
Temporal phase	Frequency	CR model	Observed	CR model	Observed
No energy injection ($<\sim 3 \times 10^4$ s)	X-ray ($\nu > \nu_c$)	1.32	1.53 ± 0.14	1.21	$1.16^{+0.24}_{-0.23}$
	optical ($\nu_m < \nu < \nu_c$)	1.07	0.94 ± 0.16	0.71	0.75 ± 0.39
Energy injection $q = 0.3$ ($>\sim 3 \times 10^4$ s)	X-ray ($\nu > \nu_c$)	0.48	0.48 ± 0.12	1.21	1.10 ± 0.13
	optical ($\nu_m < \nu < \nu_c$)	0.04	–	0.71	–
	radio ($\nu_a < \nu < \nu_m$)	−1.13	~ -0.94	−0.33-	–

Table 6. Resulting parameters from the SN model (equation (6)) fitting to the optical data beyond 1 day ($t > 86400$s).

SN model parameters	t_0 (s)	$\tau_{\rm rise}$ (s)	$\tau_{\rm fall}$ (s)	A	c
Fitting results	$(1.596 \pm 0.088) \times 10^6$	$(1.17 \pm 0.35) \times 10^5$	$(1.37 \pm 0.49) \times 10^5$	$(9.8 \pm 2.4) \times 10^{-6}$	$(9.2 \pm 3.4) \times 10^{-7}$

The result of the fitting is given in Table 6 with 1σ errors, and presented in the light curve in Fig. 1. Based on the t_0, $\tau_{\rm fall}$ and $\tau_{\rm rise}$ values, the peak of the supernova is at $t_{\rm peak} = (1.4 \pm 0.4) \times 10^6$ s $= 16 \pm 5$ d. The definition for the rise time given in Taddia et al. (2015) is $t_{\rm rise} = t_{\rm peak} - t_{\rm expl}$ where $t_{\rm expl}$ is the average between the last non-detection of the supernova and the first detection point. Since we have observed the GRB and all times are given relative to the trigger time, by definition $t_{\rm expl} = 0$, and $t_{\rm rise} = t_{\rm peak}$. The observed rise time of the SN converted to the rest frame of the GRB is $t_{\rm rise} = 11.3 \pm 3.5$ d. Based on the results from Taddia et al. (2015), this is within the 50$^{\rm th}$ percentile for SNe Ic and within the 11$^{\rm th}$ percentile for SNe Ic-BL. Taddia et al. (2015) shows that SNe Ib or IIb have rise times $15 \lesssim t_{\rm rise} \lesssim 30$, making this SN more consistent with type Ic and Ic-BL.

The peak luminosity of the SN from our fits was $(7 \pm 5) \times 10^{-6}$ Jy, or 21.7 ± 0.7 mag, assuming a luminosity distance $D_{\rm L} = 2520.1$ Mpc, we have an absolute magnitude of $M_{\rm R} = -20.3 \pm 0.7$ mag. Lyman, Bersier & James (2014) show that the bolometric correction for Type I core-collapse supernovae to V–band (approximate rest-frame of our observed R–band) around peak is close to zero (typically from -0.2 to 0.7 mag), and so our R–band peak luminosity can be approximated to bolometric. Peak bolometric magnitudes range from approximately -16 to -19 mag for Type Ic-BL SNe (Lyman et al. 2016; Prentice et al. 2019). Although this indicates the SN associated with GRB 201015A was somewhat luminous in comparison, other luminous examples of GRB-SNe exist such as SN2011kl (Kann et al. 2016) and SN2012bz (Schulze et al. 2014) and are more comparable with peak luminosities $M_{\rm V} = -19.28$ mag and $M_{\rm V} = -19.7$ mag respectively. SN2011kl is spectrally more similar to a super-luminous SN (SLSN) than other GRB-SNe, and it is associated with a ultra-long GRB (111209A) Greiner et al. (2015). Whereas SN2012bz is the counterpart of GRB 120422A, a relatively low-luminosity GRB with a $T_{90} = 5.4 \pm 1.4$ s and $E_{\gamma,\rm iso}$=$(1.6 - -3.2) \times 10^{50}$ erg Schulze et al. (2014), and hence quite comparable to GRB 201015A. Given our large statistical uncertainty on the peak, and an additional bolometric correction systematic uncertainty, we cannot analyse the luminosity of the SN associated with GRB 201015A beyond these general statements.

3.3 Dainotti relation

The canonical X-ray afterglow of GRBs contains a plateau phase where the decay constant increases, which is typically linked to energy injection (Nousek et al. 2006). In the afterglow of GRB 201015A, the energy injection phase is seen to last surprisingly long and there is no visible end time. The 3D Dainotti relation links the end time of the plateau phase in the afterglow ($T_{\rm a}$), with the end of plateau X-ray luminosity ($L_{\rm a}$), and with the luminosity of the brightest second of the GRB prompt emission ($L_{\rm p}$) (Dainotti et al. 2017). Since we do not know where the end of the plateau phase is, the separate 2D relations given in Dainotti et al. (2015) were used in order to get a prediction of $T_{\rm a}$ and test if this afterglow violates the Dainotti relation. Combining the following equations from Dainotti et al. (2015):

$$\log(L_{\rm a}) = A + B\log(L_{\rm p}) \tag{8}$$

$$\log(L_{\rm a}) = \log(a) + b\log(T_{\rm a}) \tag{9}$$

gives:

$$\log(T_{\rm a}) = \frac{A + B\log(L_{\rm p}) - \log(a)}{b} \tag{10}$$

where $A = -14.67 \pm 3.46$, $B = 1.21^{+0.14}_{-0.13}$, $b = -0.90^{+0.19}_{-0.17}$, $\log(a) = 51.14 \pm 0.58$. The peak luminosity, $L_{\rm p} = (5.81^{+1.68}_{-1.53}) \times 10^{49}$ erg s^{-1}, was found from the peak 1 second spectrum of the prompt emission of GRB 201015A, created using the automated HEASoft BATGRBPRODUCT processing. Using equation (10), we find $T_a = 1.67^{+1.14}_{-0.65} \times 10^6$ s. This result is represented in Fig. 1 by the position of the pink arrow, and the 1σ confidence region is indicated by the dash-dotted pink horizontal line.

The position of the predicted end time of the plateau falls closely with the last XRT observation. This long-lasting, and late shallow plateau phase could be a normal feature of a burst with a low $E_{\gamma,\rm iso}$ assuming these bursts follow the Dainotti relation, however we have not observed many late plateaux.

3.4 Jet opening angle

The observation of a jet break – a shallow-to-steep transition in the light curve – is a useful feature which the majority of GRB observations do not have (Racusin et al. 2009). Based on the estimated end time for the X-ray plateau, we estimate the lower limit for the jet half opening angle, $\theta_{\rm j}$. Here we assume the jet break time is $t_{\rm j} \geq 1.76 \times 10^6$ s =20.4 d, as this is the time of the last measurement in the X-ray band. The start time of the energy injection is estimated as $t_{\rm i} = (2.61 \pm 1.27) \times 10^4$ s =0.3 d based on the broken power-law fit to the X-ray light curve. Since we are finding the lower limit for $\theta_{\rm j}$, we approximate the circumburst density to be $n_0 = 0.1$ taking the lower value from the range of $n_0 = 0.1$–100 cm^{-3} for long GRBs given in Panaitescu & Kumar (2002). The energy injection parameter has been converted from the q-value to the s-value for the shell model using the conversion equation for the ISM shock model in Zhang et al. (2006):

$$s = \frac{10 - 7q}{2 + q} \tag{11}$$

giving $s = 3.7$ for $q = 0.24$. The initial isotropic kinetic energy of the burst is given by:

$$E_{\rm K,iso} = E_{\gamma,\rm iso}\left(\frac{1}{\eta_\gamma} - 1\right) \tag{12}$$

hence $E_{\rm K} \sim 0.158 \times 10^{52}$ erg if we take η_γ to be approximately 0.1. To calculate the total kinetic energy we use the following equation:

$$E_{\rm K,final} = E_{\rm K,intial}\left(\frac{t_f}{t_i}\right)^{3(s-1)/(7+s)} \tag{13}$$

providing the final isotropic kinetic energy $E_{\rm K} \sim 3.8 \times 10^{52}$ erg. Finally, using the equation for half jet opening angle in Fong et al. (2014):

$$\theta_j = 9.51 t_{\rm j,d}^{3/8}(1+z)^{-3/8} E_{\rm K,iso,52}^{-1/8} n_0^{1/8} \deg \tag{14}$$

Table 7. Tabulated values for the bursts of interest in the low-$E_{\rm peak}$ and low-$E_{\gamma,\rm iso}$ section of the Amati plot. The T_{90} values have been gathered from GCN notices, except 060218, which was from Campana et al. (2006). We calculated the $E_{\gamma,\rm iso}$ and $E_{\rm peak}$ using XSPEC unless already provided in Amati (2006). The BAT and XRT photon indices were also calculated using XSPEC, except for 060218, which was gathered from the third *Swift*-BAT catalogue (Lien et al. 2016) and the *Swift* Burst Analyser (Evans et al. 2010).

GRB	Redshift	T_{90} (s)	$E_{\gamma,\rm iso}$ ($\times 10^{50}$ erg)	$E_{\rm p}$ (keV)	BAT photon index	XRT spectra photon index
201015A	0.426	9.78 ± 3.47	$1.75^{+0.60}_{-0.53}$	<21.39	$3.00^{+0.50}_{-0.42}$	$2.16^{+0.41}_{-0.36}$
140622A	0.959	0.13 ± 0.04	0.79 ± 0.18	87.3^{+77}_{-63}	$3.17^{+0.20}_{-0.17}$	1.70 ± 0.50
080520	1.55	3.32 ± 0.86	$7.10^{+1.73}_{-1.65}$	<38.25	$3.14^{+0.42}_{-0.35}$	$2.10^{+0.33}_{-0.31}$
060218	0.033	2100 ± 100[9]	0.534 ± 0.053	4.9 ± 0.49	$2.18^{+0.20}_{-0.18}$	1.67 ± 0.01
050416A	0.6535	6.7 ± 3.4	$10.3^{+1.7}_{-1.7}$	$22.0^{+4.5}_{-4.5}$	$3.27^{+0.21}_{-0.19}$	$1.96^{+0.10}_{-0.09}$
020903	0.25	$\sim$3.3	0.24 ± 0.06	3.37 ± 1.79	-	-

shows that $\theta_{\rm j} \geq 16^\circ$. This value of $\theta_{\rm j}$ is consistent with the population of long GRBs which have a range of $2^\circ < \theta_{\rm j} < 25^\circ$, although it is greater than the mean of $\theta_{\rm j} = 7^\circ$ (Fong et al. 2014). We have treated this as a uniform jet, but other jet structures and components (e.g. cocoon) may provide different results Lamb et al. (2021b).

Assuming the half jet opening angle, $\theta_{\rm j} = 16^\circ$, we can estimate the energy emitted in gamma-rays from the prompt emission of this GRB. The $E_{\gamma,\rm iso}$ is corrected by the beaming factor (Peng, Königl & Granot 2005):

$$E_\gamma = E_{\gamma,\rm iso}\left(\frac{\theta_j^2}{2}\right) \tag{15}$$

giving $E_\gamma \sim 6.7^{+2.3}_{-2.0} \times 10^{48}$ erg.

4 COMPARISON TO THE SPECTRALLY SOFT POPULATION

Only three GRBs in the third *Swift*-BAT catalogue (Lien et al. 2016) have a prompt emission spectrum with photon indices $\Gamma > 3$: 050416A, 080 520 and 140622A. From this sample, 140622A is the only GRB thought to have a merger progenitor, based on the duration $T_{90} = 0.13 \pm 0.04$ s, although this characterization as a short GRB is uncertain based on its unusually soft spectrum (Sakamoto et al. 2014). Machine learning analysis of the prompt emission also categorizes it as a short GRB (Jespersen et al. 2020). The others have been classified as long GRBs based on their T_{90} being greater than 2 s and having a soft spectrum, however without the observation of a supernova or kilonova counterpart, these classifications cannot be confirmed.

We fit the BAT T_{100} spectra from the third *Swift*-BAT catalogue (Lien et al. 2016), and XRT time-averaged spectra from the *Swift* Burst Analyser[8] (Evans et al. 2010) to a simple power-law model to find the photon indices. We find that the photon indices for both the BAT and XRT bands are similar for each of the GRBs: $\Gamma_{\rm BAT} \sim 3$ and $\Gamma_{\rm XRT} \sim 2$. The values of each of the photon indices can be found on Table 7.

The Amati relation provides a correlation between $E_{\rm p}$ and $E_{\gamma,\rm iso}$ of the time-averaged prompt spectrum of long GRBs (Amati et al. 2002). In order to check the $E_{\rm p}$ and $E_{\gamma,\rm iso}$ of this sample of GRBs relative to the Amati relation, we have selected the best-fitting model from a simple power-law, cut-off power-law, and Band function fit to the T_{100} BAT spectra. The method used is as described in Section 2.2 for GRB 201015A, where the equation for the spectral peak energy (equation (1)) uses the low-energy spectral index (β_1) in the case of the Band function. The values calculated for GRB 201015A and the other 3 GRBs in this sample were plotted onto an Amati plot (Fig. 2) with a large sample of long GRBs with well-measured redshift and spectral parameters (Amati 2006), as well as a few *Swift* short GRBs for comparison (D'Avanzo et al. 2014). We have an upper limit for $E_{\rm p}$ in the case of GRB 201015A and GRB 080 520 because the cut-off power-law or Band function could not be adequately fit to their spectra using XSPEC. The lower-limit for the bandpass of the BAT detector (15 keV) was considered the upper limit for the break, and then converted to the rest frame of the GRB using the redshifts of the GRBs. Fig. 2 clearly indicates that these bursts along with two others (060218 and 020903) are outliers in terms of their low-$E_{\gamma,\rm iso}$ and low-$E_{\rm p}$ compared to the rest of the population, but they still fit the Amati relation. The findings for these low-$E_{\rm p}$ and low-$E_{\gamma,\rm iso}$ events are shown in Table 7. We find that this population is of low redshift with 5 out of 6 GRBs having a redshift of $z < 1$. Most of the GRBs have short time-scales $T_{90} < 10$ s, apart from the GRB 060 218 T_{90} calculated by Campana et al. (2006).

We have used the data from the *Swift* BAT catalogue (Lien et al. 2016) to plot these GRBs on a plot of T_{90} against hardness ratio (HR). To find HR, we have used the simple power-law fit for all the GRBs in the sample to calculate the ratio of the fluence in the 50–100 keV band to the 25–50 keV band. For GRB 190326A, there was no error provided for the fluence or the fit parameters. Fig. 3 shows the scatter plot of the T_{90} and HR values, with histograms of both distributions. By fitting a Gaussian curve to the HR distribution, we find that the HR for GRB 201015A is 3.4σ from the mean and the GRB 140622A HR of 0.62 is 2.5σ from the mean. In Table 8, we have tabulated a list of soft GRBs with HR $\leq$0.62 and $T_{90} < 10$ s, with information on the classification of the GRBs and their redshift found from GCN circulars. The sample of soft GRBs are a mix of mergers and collapsars, with shorter durations than the the general population of short and long GRBs respectively. These GRBs are also found at lower redshifts than most detected GRBs, since only 10 per cent of GRBs have $z < 1$ (Le & Mehta 2017).

The sample of low-luminosity soft GRBs detected by *Swift* do not seem to show any similarity in their morphology in the prompt emission light curves. To compare their X-ray afterglows, we have plotted their afterglow light curves in Fig. 4 showing the flux in the 0.3–10.0 keV band, along with all *Swift* GRBs followed up by XRT. This plot was created using the SWIFTTOOLS API[10] (Evans

[8] https://www.swift.ac.uk/burst_analyser/
[9] (Campana et al. 2006).
[10] https://www.swift.ac.uk/API

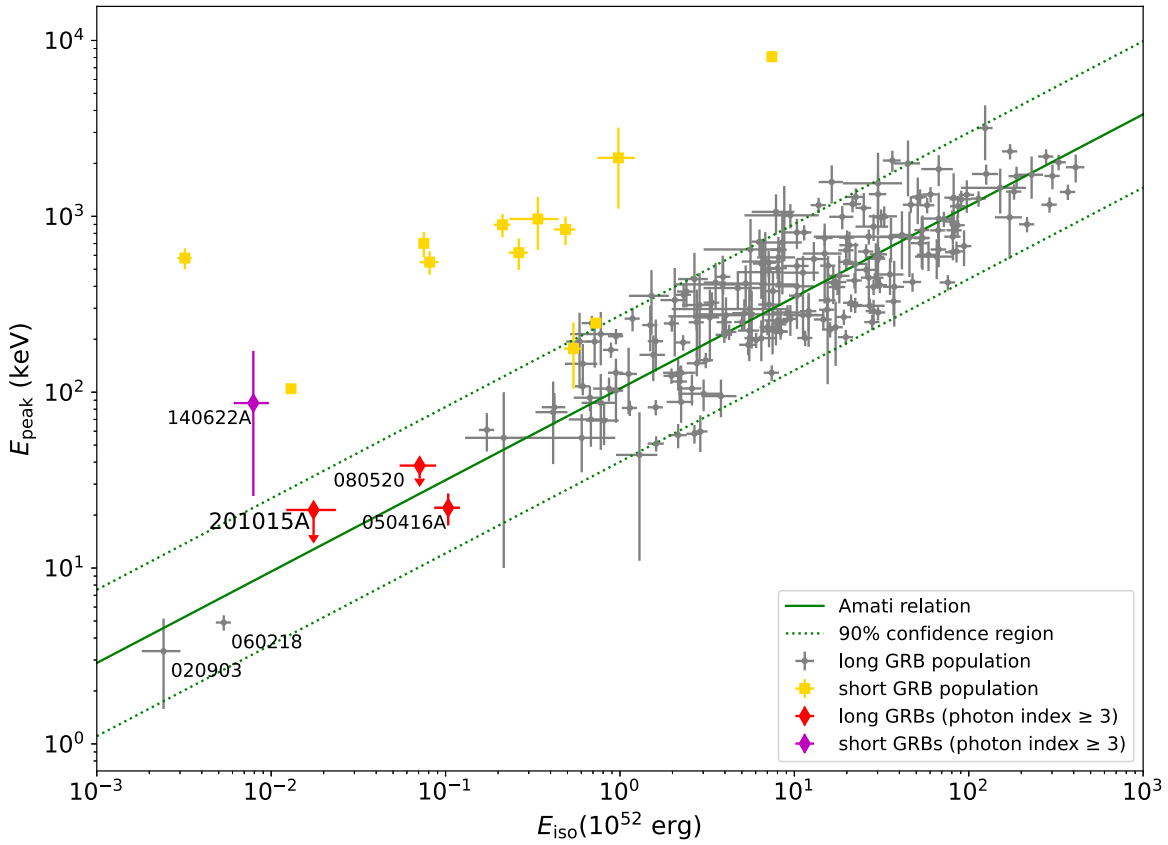

Figure 2. The equivalent isotropic energy $E_{\gamma,\rm iso}$ (10^{52} erg) of GRBs plotted against their spectral peak energy $E_{\rm p}$ (keV), showing the correlation known as the Amati relation (green lines; Amati 2006). The grey points represent the general population of long GRBs detected by various instruments, and the yellow squares represent the short *Swift* GRBs presented in D'Avanzo et al. (2014). The spectrally soft sample of GRBs with photon index (Γ) ≥ 3 is marked in red for long GRBs and purple for short GRBs.

et al. 2007). The median light curve of short GRBs (yellow) is lower than that of long GRBs (grey) as shown in Margutti et al. (2013). This figure shows that the low-$E_{\rm p}$ and low-$E_{\gamma,\rm iso}$ long GRBs (red) typically have X-ray afterglows with lower flux than the median of the population of long GRBs, and are more in line with the short GRB median light curve. The short GRB 140822A (purple) only has one data point, which is also lower in flux than the median for short GRBs, however this is not enough data to draw conclusions. The outlier in the low-$E_{\rm p}$ and low-$E_{\gamma,\rm iso}$ long GRBs is 060 218 which is more luminous in the 0.3–10.0 keV range than the other GRBs in red up to $\sim 10^4$ s after which it joins the others. This emission has been attributed to the prompt emission of the GRB rather than the afterglow since it has $T_{90} = 2100 \pm 100$ s (Campana et al. 2006).

GRB 060 218 has a remarkably low redshift of $z = 0.033$, but is the outlier in terms of the T_{90}. The duration of the burst is unclear based on the BATGRBPRODUCT automated analysis[11], but Campana et al. (2006) has determined $T_{90} = 2100 \pm 100$ s for this burst. It is believed to be off-axis by a few degrees based on the inner fast variability being attributed to a precessing jet (Fargion 2006). This GRB was associated with supernova SN 2006aj based on the continuum spectrum of the optical transient detected by VLT (N. Masetti, Pian & Patat 2006). The underluminous nature of this burst and the detection of a thermal component in the X-ray is interpreted as a mildly relativistic jet causing a shock breakout into dense circumstellar material (Campana et al. 2006; Nakar 2015). An alternative model suggests a low-luminosity low Lorentz factor jet ($\gamma = 10$) with a low-mass circumstellar envelope, and extinction due to dust (Irwin & Chevalier 2016). GRB 100316D is an analogous burst to GRB 060 218 with a low $E_{\rm peak}$ in the range of 10–42 keV (90 per cent confidence range) and an estimated $E_{\gamma,\rm iso} \geq (5.9 \pm 0.5) \times 10^{49}$ erg (Starling et al. 2011). Unlike these GRBs, the spectrum of GRB 201015A is not well fitted with a blackbody, making it unlikely to have a thermal component.

XRF 020903, a transient detected in the 2–5 keV band by the WXM instrument on HETE observing in the 2–30 keV range (Ricker et al. 2002), was categorized as an X-ray Flash (XRF) due to its extremely low $E_{\rm p}$ of 3.37 ± 1.79 (Soderberg et al. 2004). The event coincided with a SN confirmed by the rebrightening in the optical at 24 d and spectroscopic follow up of the optical transient (Soderberg et al. 2002). Urata et al. (2015) studied the afterglow light curve discovering the achromatic rebrightening hence the off-axis viewing. Therefore this event is considered to be an off-axis orphan GRB, for which the narrow collimated relativistic jet is not seen, but the wider afterglow signal can still be detected. This is expected to be observed for GRBs with $\theta_{\rm obs} > 20^\circ$ (Urata et al. 2015). Furthermore, spectroscopic observations into the host galaxy of XRF 020 903 with ALMA identified similar properties to GRB host galaxies, supporting the origin of this event to be the same as long GRBs (Chen, Urata & Huang 2021).

[11] https://gcn.gsfc.nasa.gov/notices_s/191157/BA

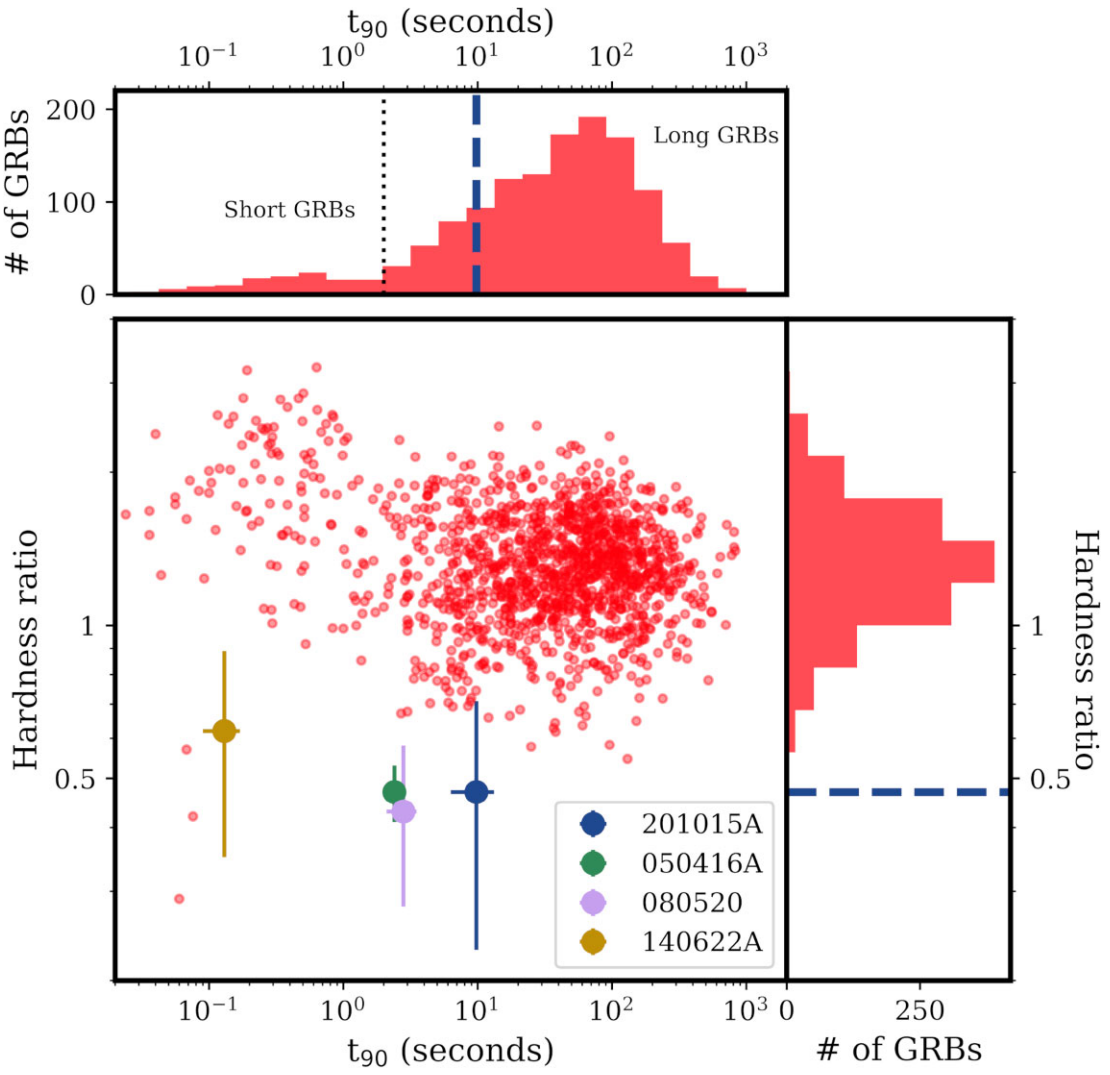

Figure 3. Plot of T_{90} against the hardness ratio (fluence in 50–100 keV band over fluence in 25–50 keV band from the power-law fit) of GRBs from the third *Swift*-BAT catalogue (Lien et al. 2016). The GRBs with photon index $\Gamma > 3$ are coloured differently on the plot and labelled in the legend. The histograms of T_{90} and HR are shown on the top and right sides of the plot, with the properties of GRB 201015A highlighted with a dashed blue line.

Table 8. List of soft GRBs in the BAT catalogue with a low hardness ratio (<0.6) and T_{90} less than 10s (Lien et al. 2016), with redshift information collected from GCN notices.

GRB	T_{90} (s)	HR	classification	redshift
050416A	2.49 ± 0.44	0.44 ± 0.06	long	0.6535
080520	2.82 ± 0.66	0.43 ± 0.15	long	1.545
090417A	0.068 ± 0.022	$0.57^{+0.15}_{-0.16}$	short	0.088
140622A	0.13 ± 0.04	0.62 ± 0.27	short	0.959
150101A	0.060 ± 0.011	0.29 ± 0.16	short	-
180718A	0.084 ± 0.023	0.16 ± 0.09	short	-
190326A	0.076 ± 0.032	$0.42 \pm$N/A	short	-
201015A	9.78 ± 3.47	0.47 ± 0.15	long	0.426

5 DISCUSSION

5.1 Classification

It is not immediately clear from the high energy prompt emission observations alone whether GRB 201015A belongs in the long or short GRB category. The BAT $T_{90} = 9.78 \pm 3.47$ s is consistent with a long burst, whereas the sub-threshold detection by *Fermi* GBM provides 1.024 s as an estimate of the duration. This emphasizes the uncertainty in the measured duration of the bursts based on the detector bandpass, and how this can lead to incorrect categorization based on T_{90}. The *Swift* BAT bandpass is 15–150 keV (Gehrels et al. 2004), whereas *Fermi* has a larger effective energy range of 8 keV–40 MeV (Yu et al. 2016).

The upper limit of $E_{\rm p}$ and value of $E_{\gamma,\rm iso}$ for GRB 201015A are consistent with the 'Amati relation' for LGRBs (Amati et al. 2002; Amati 2006; Minaev & Pozanenko 2020a). However, the short pulse and extended tail morphology is more in line with a short or extended emission (EE; Norris & Bonnell 2006; Norris et al. 2010) GRB. The measured $E_{\gamma,\rm iso} = 1.75^{+0.60}_{-0.53} \times 10^{50}$ erg is under-luminous for an LGRB; the log mean $E_{\gamma,\rm iso}$ is $\sim 6.6 \times 10^{52}$ erg in the GBM-selected sample of Gompertz, Fruchter & Pe'er (2018). It is, however, more consistent with an SGRB. Mean $E_{\gamma,\rm iso}$ is $\sim 6.4 \times 10^{49}$ erg in the complete sample of SGRBs with redshift (Gompertz, Levan & Tanvir 2020). To check for consistency, we compared our independent fitting results against estimates from other sources such as GCNs, e.g.

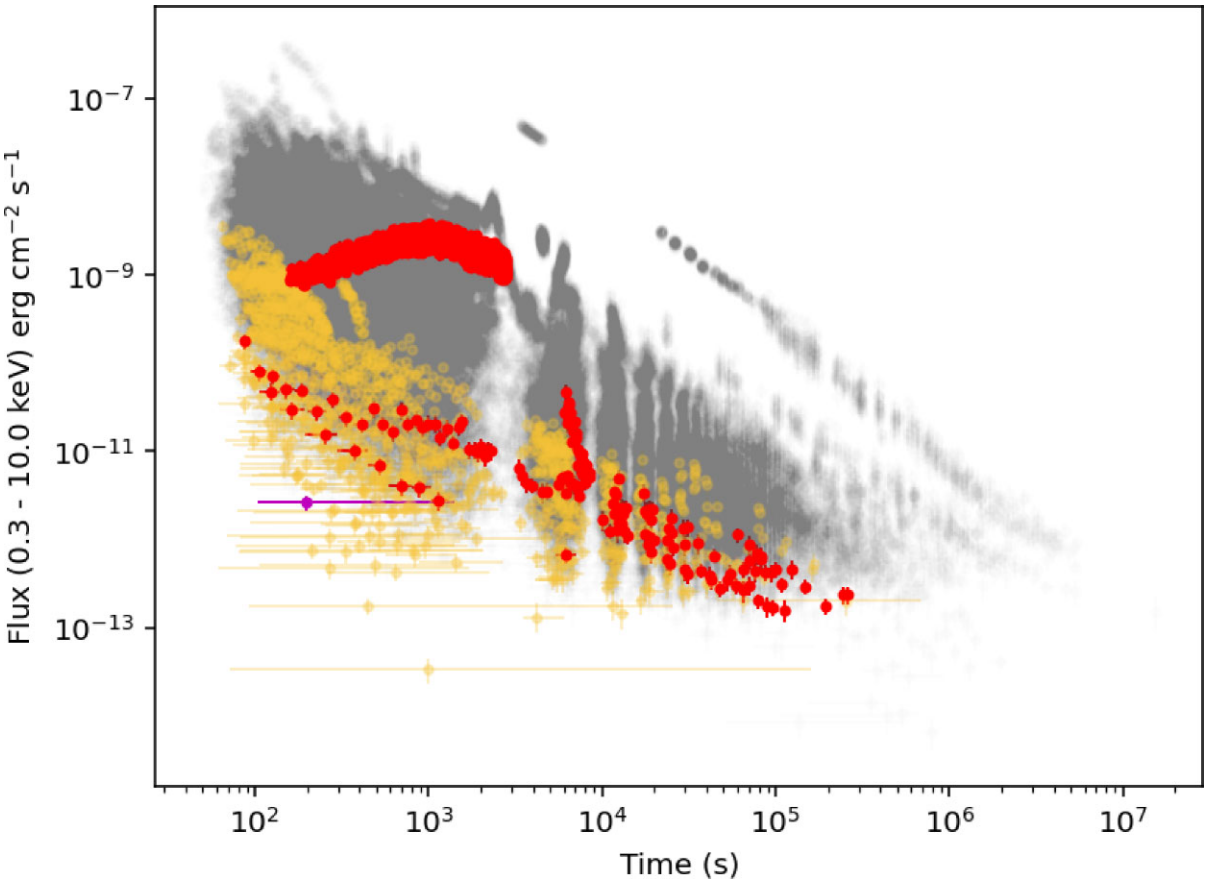

Figure 4. The XRT afterglows of *Swift* GRBs shown here are presented in flux units. This includes the light curves of GRBs 060218, 080520, 050416A, and 201015A in red, and GRB 140822A in purple, overlaid on GRBs with $T_{90} > 2$ s in grey, and GRBs with $T_{90} < 2$ s in yellow.

(Minaev & Pozanenko 2020b) for the $E_{\gamma,\rm iso}$ estimate of $\sim 10^{50}$ erg for GRB 201015A. D'Avanzo et al. (2014) and Minaev & Pozanenko (2020a) show the similar correlation for SGRBs lies just above the Amati relation for LGRBs and some SGRBs may fall closer to the LGRB relation and vice versa so this relation is not a reliable method to determine the classification of a GRB. However, the 4 bursts plotted on Fig. 2 in colour do lie in their respective regions of the $E_{\rm p}$ and $E_{\gamma,\rm iso}$ correlations, showing this relation holds in the low energy range. Given the ambiguity in the distinction of T_{90}, HR, and $E_{\gamma,\rm iso}$ for LGRBs and SGRBs, future GRBs will be difficult to classify without a supernova or kilonova counterpart to confirm their origin.

5.2 Low-luminosity soft bursts

The relative difficulty of finding bursts with low luminosity, and low spectral peak energy and their afterglows results in bursts like these going undetected by instruments designed to trigger for GRBs with high keV energies. Off-axis events for which the prompt emission may not be visible but the afterglow signal could be, might not trigger detectors and therefore have no follow up to find the afterglow other wavebands. Future missions such as SVOM and Einstein Probe will be better equipped to detect bursts in this parameter space. Einstein Probe will launch in 2023 with the intention to discover energetic transients and variable objects in the X-ray band of 0.5–4 keV with a large field of view: $60^\circ \times 60^\circ$ (Yuan et al. 2015). SVOM is also set to launch in 2023, searching for low-energy bursts in the 4–250 keV range using the Eclairs instrument with $89^\circ \times 89^\circ$ field of view, and the MXT instrument providing data in the 0.2–10 keV energy band (Bernardini, Cordier & Wei 2021). THESEUS is a potential future mission with the goal of finding high-redshift GRBs up to $z \sim 10$, possibly broadening our sample of soft GRBs at higher redshifts (Amati et al. 2021). Another proposed mission, Gamow Explorer, would trigger *JWST* and ground based telescopes for follow-up of LGRBs at $z > 6$ for spectroscopic and multiwavelength data (White 2020).

The population of GRBs exhibiting low $E_{\rm p}$ and low $E_{\gamma,\rm iso}$, are found in a scarcely populated region of the Amati plot (Fig. 2). The low luminosity could be a result of lower intrinsic energy release from these bursts, or a choked jet due to circumburst material ejected from the supernova. Alternatively these values could be explained by an off-axis viewing angle such as with the famous GRB 170817A (Lamb, Levan & Tanvir 2020) or more recently GRB 190829A (Sato et al. 2021). XRF 020 903 also shows evidence of off-axis viewing based on the achromatic rebrightening and is considered an off-axis orphan afterglow (Urata et al. 2015). The off-axis model should reduce the flux, but not affect the photon index of the GRB. It does however lower the characteristic frequency making the overall spectrum softer, and can make the observed photon index softer if the characteristic frequency is shifted across the observational energy band (Lamb et al. 2021a). For GRB 201015A, we cannot find evidence of achromatic rebrightening so the jet is not considered to be off-axis.In the case of GRB 060218, it is considered to be a result of a shock breakout into a dense circumburst environment by

Campana et al. (2006); Nakar (2015), but interpretted as a lower Lorentz factor jet by Irwin & Chevalier (2016) which makes the outflow more opaque to the gamma-rays. The shock breakout model should not affect the photon index of the prompt emission of the GRB, so this provides an explanation of why this GRB has $\Gamma = 2.18^{+0.20}_{-0.18}$, a more typical value compared to $\Gamma \geq 3$ (Irwin & Chevalier 2016).GRB 060 218 is thought to be off-axis by a few degrees, with the precession of the jet resulting in rebrightening and variation in the optical and radio afterglows observed (Fargion 2006). For GRB 201015A there is no evidence of a shock breakout based on the spectral fitting, and it is difficult to determine whether there is rebrightening in the optical at the same time as the X-ray rebrightening due to the SN, indicating the most likely scenario is that of an intrinsically low-luminosity jet. The relatively large half jet opening angle estimated to be $\theta_j > 16^\circ$ suggested it is a poorly collimated jet. We find that there are various scenarios which make GRBs appear to have low-$E_{\gamma,\rm iso}$, and for all these GRBs, follow-up observations are required to understand the nature of what is causing the lower luminosity.

5.3 Follow-up observations

Based on the closure relations found to best fit the temporal and spectral indices measured for GRB 201015, we find that the energy injection scenario is the most plausible for explaining the X-ray light curve. GRB 130603B was also found to have energy injection characterized by $q = 0.3$, but the radio data does not fit the energy injection model leading to the magnetar spin-down scenario being the best explanation (Fong et al. 2014). Treating the shallowing of GRB 201015A as a normal GRB X-ray afterglow plateau, which is a phase linked to energy injection (Bernardini et al. 2012), shows that it does not violate the Dianotti relation even though it is a very late plateau (Dainotti et al. 2015). It is difficult to explain the origin of this central engine activity and some relate this phase to slightly off-axis viewing (Beniamini et al. 2020). The closure relation described in Section 3.1 fits the afterglow very well, this is partially due to the energy injection coefficient chosen to match the X-ray data after the beginning of the plateau, but this also fits remarkably well with the radio observations, supporting the scenario of ongoing central activity at late-time from this GRB. The earlier phase of X-ray data seems to lie above the prediction from the closure relation which could be an indication of flares from central engine activity as commonly seen in some *Swift* GRBs (Zhang et al. 2006).

The TeV emission detected from GRBs is considered independent to the prompt emission as it is most likely produced by inverse Compton of the afterglow (Zhang et al. 2020b), therefore we cannot explain the VHE emission with the models proposed for the low-energy soft GRBs. More observations of GRBs in VHE are required for further study with comparisons of the afterglows, and prompt emission of VHE GRBs. We have attempted to account for the variation in observations in the different optical bands using the zero points of the filters (Frei & Gunn 1994), after adjusting for Galactic extinction and absorption based on assumed models for the wavelengths (Schlafly & Finkbeiner 2011), but it is difficult to account for host galaxy reddening because the extinction curve is unknown. This can also affect the measured optical spectral index we have used to infer the closure relations for this GRB.

Due to the ambiguous prompt emission, the follow-up observations in the optical showing evidence of a SN were necessary to identifying the classification of this burst. This GRB highlights the importance of follow-up missions in categorizing GRBs and studying their jets and environments.

6 CONCLUSIONS

GRB 201015A is an interesting long GRB for many reasons. It is the fifth burst to have a candidate VHE detection, and is the burst with the lowest prompt energy out of this group. It has a surprisingly low luminosity for a GRB with isotropic energy $E_{\gamma,\rm iso} = 1.75^{+0.60}_{-0.53} \times 10^{50}$ erg, and $E_\gamma \sim 6.7^{+2.3}_{-2.0} \times 10^{48}$ erg based on the predicted opening angle of the jet $\theta_j \geq 17^\circ$. Relating to the low $E_{\gamma,\rm iso}$, the spectral peak energy is $E_p < 21.39$ keV, and follows the Amati relation trend for long GRBs. The burst's prompt emission spectrum is unusually soft with a photon index of $\Gamma = 3.00^{+0.50}_{-0.42}$. The hardness ratio of this GRB is 0.47 which is 3.4σ lower than the mean for *Swift* bursts.

We have compared GRB 201015A to others which are similarly spectrally soft ($\Gamma \geq 3$ and HR $\leq$0.62) from the *Swift* BAT catalogue. We find that the bursts with $\Gamma \geq 3$ are generally short-duration long GRBs which lie in the low-$E_{\rm peak}$, low-$E_{\gamma,\rm iso}$ region of the Amati plot. The sample with HR $\leq$0.62 introduces more short GRBs to our selection of soft GRBs. Both the short and long GRBs in this category tend to have a lower duration than the majority of the general short and long GRB populations, and the majority are of low redshift (all except GRB 080 520 have $z < 1$). Looking into the other GRBs in this parameter space shows that they have a range of explanations for their lower luminosity compared to the general population of GRBs. This includes off-axis viewing, shock-breakout into a denser envelope, or an intrinsically less energetic jet. The last scenario is what we have found to be the most likely for GRB 201015A due to lack of evidence for the other cases.

The afterglow of GRB 201015A was an important part of this study, since the detection of a SN in the optical bands confirmed the classification of this burst as a long GRB, and the X-ray data showed a peculiar steep-to-shallow transition at a late-time ($t_b = (2.61 \pm 1.27) \times 10^4$ s). The temporal and spectral indices found from the X-ray, optical, and some radio observations were used to match with closure relations given in Gao et al. (2013a). The best-fitting closure relations were for the relativistic, isotropic, self-similar deceleration phase for the $\nu_a < \nu_m < \nu_c$ regime in the ISM (Table 13 in Gao et al. 2013a), and electron spectral index $p = 2.42^{+0.44}_{-0.30}$. We have also matched the plateau phase to energy injection with $q = 0.24^{+0.24}_{-0.18}$ after $t = (2.61 \pm 1.27) \times 10^4$ s. The observed plateau phase of this X-ray afterglow was tested against the expected end time of the plateau T_a from the Dainotti relations, and found to be $T_a = 1.67^{+1.14}_{-1.53} \times 10^6$ s which is around the last observation in the X-ray. This shows that this GRB does not violate the Dainotti relation (Dainotti et al. 2015). We have then used the predicted T_a to constrain the lower limit of the jet half opening angle $\theta_j \geq 16^\circ$. The SN associated with this GRB has a rise time $t_{\rm rise} = 11 \pm 1$ d, consistent with type Ic and Ic-BL (Taddia et al. 2015).

With future missions such as SVOM and Einstein Probe searching in lower energy gamma-rays, and X-rays we will find more bursts like GRB 201015A with higher field-of-view and more sensitive instruments (Yuan et al. 2015; Bernardini et al. 2021). This will help us build a greater data set for statistical analysis of the soft GRB population. Follow-up observations of the afterglow in multiple wavelengths are also required to confirm classification of the GRB, and determine properties of the jet and environment.

ACKNOWLEDGEMENTS

MP, PO, and GPL acknowledge the support by the UKRI Science and Technology Facilities Council (STFC). BG and MN are supported by the European Research Council (ERC) under the European Union's Horizon 2020 - Research and Innovation Framework Programme

(grant agreement No. 948381). MN acknowledges a fellowship from the Alan Turing Institute. RPB acknowledges support from the ERC under 550 the European Union's Horizon 2020 - Research and Innovation Framework Programme (grant agreement No. 551 715051; Spiders).

This work makes use of data supplied by the UK *Swift* Science Data Centre at the University of Leicester and the *Neil Gehrels Swift Observatory*. This research has made use of data obtained from the Chandra Data Archive and software provided by the Chandra X-ray Center (CXC) in the application packages CIAO and Sherpa.

This work is based in part on observations taken by The Liverpool Telescope. The Liverpool Telescope is operated on the island of La Palma by Liverpool John Moores University in the Spanish Observatorio del Roque de los Muchachos of the Instituto de Astrofisica de Canarias with financial support from the UK Science and Technology Facilities Council. The Gravitational-wave Optical Transient Observer (GOTO) project acknowledges the support of the Monash-Warwick Alliance; University of Warwick; Monash University; University of Sheffield; University of Leicester; Armagh Observatory & Planetarium; the National Astronomical Research Institute of Thailand (NARIT); Instituto de Astrofísica de Canarias (IAC); University of Portsmouth; University of Turku, and the UK Science and Technology Facilities Council (STFC, grant numbers ST/T007184/1, ST/T003103/1).

DATA AVAILABILITY

The data underlying this article will be shared on reasonable request to the corresponding author.

REFERENCES

Abbott B. P. et al., 2017, ApJ, 848, L13
Ackley K. et al., 2020, GCN Circ., 28639, 1
Ahumada T. et al., 2021, Nat. Astron., 5, 917
Amati L. et al., 2002, A&A, 390, 81
Amati L. et al., 2021, Exp. Astron., 52, 183
Amati L., 2006, MNRAS, 372, 233
Amati L., 2021, Nat. Astron., 5, 877
Arnaud K. A., 1996, in Jacoby G. H., Barnes J., eds, ASP Conf. Ser. Vol. 101, Astronomical Data Analysis Software and Systems V. Astron. Soc. Pac., San Francisco, p. 17
Band D. et al., 1993, ApJ, 413, 281
Barbary K., 2016, J. Open Source Softw., 1, 58
Barthelmy S. D. et al., 2005, Space Sci. Rev., 120, 143
Bazin G. et al., 2011, A&A, 534, A43
Beniamini P., Duque R., Daigne F., Mochkovitch R., 2020, MNRAS, 492, 2847
Beniamini P., van der Horst A. J., 2017, MNRAS, 472, 3161
Bernardini M. G., Cordier B., Wei J., 2021, Galaxies, 9, 113
Bernardini M. G., Margutti R., Mao J., Zaninoni E., Chincarini G., 2012, A&A, 539, A3
Berti A., Carosi A., 2022, Galaxies, 10, 67
Bertin E., Arnouts S., 1996, A&AS, 117, 393
Blanch O. et al., 2020, GCN Circ., 28659, 1
Burrows D. N. et al., 2005, Science, 309, 1833
Campana S. et al., 2006, Nature, 442, 1008
Cash W., 1979, ApJ, 228, 939
Chambers K. C. et al., 2016, preprint (arXiv:1612.05560)
Chen J.-C., Urata Y., Huang K., 2021, ApJ, 915, 46
Chen W., Xie W., Lei W.-H., Zou Y.-C., Lü H.-J., Liang E.-W., Gao H., Wang D.-X., 2017, ApJ, 849, 119
Chevalier R. A., Li Z.-Y., 1999, ApJ, 520, L29
D'Avanzo P. et al., 2014, MNRAS, 442, 2342
D'Elia V. et al., 2020, GCN Circ., 28632, 1
Dainotti M. G., Hernandez X., Postnikov S., Nagataki S., O'brien P., Willingale R., Striegel S., 2017, ApJ, 848, 88
Dainotti M., Petrosian V., Willingale R., O'Brien P., Ostrowski M., Nagataki S., 2015, MNRAS, 451, 3898
de Ugarte Postigo A., Kann D. A., Blazek M., Agui Fernandez J. F., Thoene C., Gomez Velarde G., 2020, GCN Circ., 28649, 1
Evans P. A. et al., 2007, A&A, 469, 379
Evans P. A. et al., 2009, MNRAS, 397, 1177
Evans P. A. et al., 2010, A&A, 519, A102
Evans P. A., Goad M. R., Osborne J. P., Beardmore A. P., Swift-XRT Team., 2020, GCN Circ., 28647, 1
Fargion D., 2006, GCN Circ., 4819
Fletcher C., Veres P., Fermi-GBM Team, 2020, GCN Circ., 28663, 1
Fong W. et al., 2014, ApJ, 780, 118
Fong W. et al., 2022, ApJ, 940, 56
Fong W., Schroeder G., Rastinejad J., Hajela A., 2020, GCN Circ., 28688, 1
Frei Z., Gunn J. E., 1994, AJ, 108, 1476
Fruchter A. S. et al., 2006, Nature, 441, 463
Fukugita M., Ichikawa T., Gunn J. E., Doi M., Shimasaku K., Schneider D. P., 1996, AJ, 111, 1748
Galama T. J. et al., 1999, A&AS, 138, 465
Gao H., Lei W.-H., Zou Y.-C., Wu X.-F., Zhang B., 2013a, New Astron. Rev., 57, 141
Gao H., Ding X., Wu X.-F., Zhang B., Dai Z.-G., 2013b, ApJ, 771, 86
Gehrels N. et al., 2004, ApJ, 611, 1005
Gehrels N. et al., 2006, Nature, 444, 1044
Gehrels N. et al., 2008, ApJ, 689, 1161
Giarratana S. et al., 2022, A&A, 664, A36
Goad M. R. et al., 2007, A&A, 476, 1401
Gompertz B. P. et al., 2023, Nat. Astron., 7, 67
Gompertz B. P., Fruchter A. S., Pe'er A., 2018, ApJ, 866, 162
Gompertz B. P., Levan A. J., Tanvir N. R., 2020, ApJ, 895, 58
Greiner J. et al., 2015, Nature, 523, 189
Hjorth J. et al., 2003, Nature, 423, 847
Irwin C. M., Chevalier R. A., 2016, MNRAS, 460, 1680
Iyyani S., Ryde F., Burgess J. M., Pe'er A., Bégué D., 2016, MNRAS, 456, 2157
Jespersen C. K., Severin J. B., Steinhardt C. L., Vinther J., Fynbo J. P. U., Selsing J., Watson D., 2020, ApJ, 896, L20
Kann D. A. et al., 2016, A&A, 624, 19
Klebesadel R. W., Strong I. B., Olson R. A., 1973, ApJ, 182, L85
Kluźniak W., Ruderman M., 1998, ApJ, 505, L113
Koshut T. M., Paciesas W. S., Kouveliotou C., van Paradijs J., Pendleton G. N., Fishman G. J., Meegan C. A., 1995, BAAS, 27, 886
Kouveliotou C., Meegan C. A., Fishman G. J., Bhat N. P., Briggs M. S., Koshut T. M., Paciesas W. S., Pendleton G. N., 1993, ApJ, 413, L101
Lamb G. P. et al., 2019, ApJ, 883, 48
Lamb G. P. et al., 2021a, Universe, 7, 329
Lamb G. P., Kann D. A., Fernández J. J., Mandel I., Levan A. J., Tanvir N. R., 2021b, MNRAS, 506, 4163
Lamb G. P., Levan A. J., Tanvir N. R., 2020, ApJ, 899, 105
Lang D., Hogg D. W., Mierle K., Blanton M., Roweis S., 2010, AJ, 139, 1782
Le T., Mehta V., 2017, ApJ, 837, 17
Lei W.-H., Zhang B., Liang E.-W., 2013, ApJ, 765, 125
Levan A. J. et al., 2014, ApJ, 781, 13
Levan A., 2018, IOP Publishing. OCLC: Gamma-Ray Bursts, IOP Publishing, Bristol, UK
Levan A., Crowther P., de Grijs R., Langer N., Xu D., Yoon S.-C., 2016, Space Sci. Rev., 202, 33
Li L. et al., 2020, ApJ, 900, 176
Li L., Wu X.-F., Lei W.-H., Dai Z.-G., Liang E.-W., Ryde F., 2018, ApJS, 236, 26
Liang E., Zhang B., Virgili F., Dai Z. G., 2007, ApJ, 662, 1111
Lien A. et al., 2016, ApJ, 829, 7
Lipunov V. et al., 2010, Adv. Astron., 2010, 349171
Lipunov V. et al., 2020, GCN Circ., 28633, 1
Lü H.-J., Zhang B., Lei W.-H., Li Y., Lasky P. D., 2015, ApJ, 805, 89
Lyman J. D., Bersier D., James P. A., 2014, MNRAS, 437, 3848

Lyman J. D., Bersier D., James P. A., Mazzali P. A., Eldridge J. J., Fraser M., Pian E., 2016, MNRAS, 457, 328
Malesani D. B., de Ugarte Postigo A., Pursimo T., 2020, GCN Circ., 28637, 1
Margutti R. et al., 2013, MNRAS, 428, 729
Markwardt C. B. et al., 2020, GCN Circ., 28658, 1
Meegan C. et al., 2009, ApJ, 702, 791
Mészáros P., 2002, ARA&A, 40, 137
Minaev P. Y., Pozanenko A. S., 2020a, MNRAS, 492, 1919
Minaev P., Pozanenko A., 2020b, GCN Circ., 28668, 1
Mukherjee S., Feigelson E. D., Jogesh Babu G., Murtagh F., Fraley C., Raftery A., 1998, ApJ, 508, 314
N. Masetti E. P., Pian E., Patat F., 2006, GCN Circ., 4803
Nakar E., 2015, ApJ, 807, 172
Nava L., 2018, Int. J. Mod. Phys. D, 27, 1842003
Norris J. P., Bonnell J. T., 2006, ApJ, 643, 266
Norris J. P., Gehrels N., Scargle J. D., 2010, ApJ, 717, 411
Nousek J. A. et al., 2006, ApJ, 642, 389
Panaitescu A., Kumar P., 2002, ApJ, 571, 779
Peng F., Königl A., Granot J., 2005, ApJ, 626, 966
Piran T., 2005, Rev. Mod. Phys., 76, 1143
Prentice S. J. et al., 2019, MNRAS, 485, 1559
Racusin J. L. et al., 2009, ApJ, 698, 43
Rastinejad J. C. et al., 2022, Nature, 612, 223
Rastinejad J., Paterson K., Kilpatrick C. D., Fong W., 2020, GCN Circ., 28676, 1
Rhodes L., Fender R., Bray J., Williams D. R. A., 2020, GCN Circ., 28945, 1
Ricker G., Atteia J.-L., Kawai N., Lamb D., Woosley S., 2002, GCN Circ., 1530
Rossi A., Benetti S., Palazzi E., D'Avanzo P., D'Elia V., De Pasquale M., CIBO Collaboration, 2021, GCN Circ., 29306, 1
Sakamoto T. et al., 2014, GCN Circ., 16438
Sari R., Piran T., Halpern J. P., 1999, ApJ, 519, L17
Sari R., Piran T., Narayan R., 1998, ApJ, 497, L17
Sato Y., Obayashi K., Yamazaki R., Murase K., Ohira Y., 2021, MNRAS, 504, 5647
Schlafly E. F., Finkbeiner D. P., 2011, ApJ, 737, 103
Schulze S. et al., 2014, A&A, 566, A102
Soderberg A. M. et al., 2004, ApJ, 606, 994
Soderberg A., Price P., Fox D., Kulkarni S., Djorgovski S., Berger E., Harrison F., Yost S., 2002, GCN Circ., 1554
Stanek K. Z. et al., 2003, ApJ, 591, L17
Starling R. L. C. et al., 2011, MNRAS, 411, 2792
Steeghs D. et al., 2022, MNRAS, 511, 2405
Steele I. A. et al., 2004, Proc. SPIE, 5489, 679
Suda Y. et al., 2021, Proc. Sci., Observation of a Relatively Low Luminosity Long Duration GRB 201015A by the MAGIC Telescopes. SISSA, Trieste, PoS(ICRC2021)797
Taddia F. et al., 2015, A&A, 574, A60
Tang C.-H., Huang Y.-F., Geng J.-J., Zhang Z.-B., 2019, ApJS, 245, 1
Tanvir N. R., Levan A. J., Fruchter A. S., Hjorth J., Hounsell R. A., Wiersema K., Tunnicliffe R. L., 2013, Nature, 500, 547
Tonry J. L. et al., 2018, ApJ, 867, 105
Troja E. et al., 2017, Nature, 551, 71
Troja E. et al., 2018, Nat. Commun., 9, 4089
Tunnicliffe R. L., Levan A., 2012, in Roming P., Kawai N., Pian E., eds, Proc. IAU Symp., Vol. 279, Death of Massive Stars: Supernovae and Gamma-Ray Bursts. Cambridge Univ. Press, Cambridge, p. 415
Urata Y., Huang K., Yamazaki R., Sakamoto T., 2015, ApJ, 806, 222
Virgili F. J., Liang E.-W., Zhang B., 2008, MNRAS, 392, 91
White N. E., 2020, in Sakamoto T., Serino M., Sugta S., eds, Proc. Conf., Yamada Conference LXXI: Gamma-ray Bursts in the Gravitational Wave Era 2019. p. 51
Willingale R., Starling R. L. C., Beardmore A. P., Tanvir N. R., O'Brien P. T., 2013, MNRAS, 431, 394
Wilms J., Allen A., McCray R., 2000, ApJ, 542, 914
Yu H.-F. et al., 2016, A&A, 588, A135
Yuan W. et al., 2015, preprint (arXiv:1506.07735)
Zhang B., Fan Y. Z., Dyks J., Kobayashi S., Mészáros P., Burrows D. N., Nousek J. A., Gehrels N., 2006, ApJ, 642, 354
Zhang B., Lü H.-J., Liang E.-W., 2016, Space Sci. Rev., 202, 3
Zhang B., Mészáros P., 2001, ApJ, 552, L35
Zhang B., Mészáros P., 2004, Int. J. Mod. Phys. A, 19, 2385
Zhang B.-B. et al., 2021, Nat. Astron., 5, 911
Zhang H., Christie I. M., Petropoulou M., Rueda-Becerril J. M., Giannios D., 2020b, MNRAS, 496, 974
Zhang X.-L., Zhang C.-T., Li X.-J., Su F.-F., Dong X.-F., Chang H.-Y., Zhang Z.-B., 2020a, Res. Astron. Astrophys., 20, 201
Zhang Z. B., Jiang M., Zhang Y., Zhang K., Li X. J., Zhang Q., 2020c, ApJ, 902, 40

SUPPORTING INFORMATION

Supplementary data are available at *MNRAS* online.

suppl_data

Please note: Oxford University Press is not responsible for the content or functionality of any supporting materials supplied by the authors. Any queries (other than missing material) should be directed to the corresponding author for the article.

APPENDIX

The optical afterglow and supernova observations plotted in Fig. 1 are given in Table S1 of the Supoporting Information, and a sample of the table is shown below (Table A1). These data were used for the power-law/broken power-law, and SN model fitting. The results from the fitting were used to determine the spectral and temporal indices, deceleration time of the afterglow, and SN peak time and luminosity.

Table A1. This table lists a sample of the optical data on GRB 201015A used for analysis in this paper. The rest of the data can be found in the Supporting Information.

time(s)	observed magnitude	err low	err high	filter	telescope	GCN
73.2	17.67	0.1	0.1	i'	NUTTelA-TAO/BSTI	28674
73.2	17.79	0.1	0.1	r'	NUTTelA-TAO/BSTI	28674
98.0	18.34	0.08	0.08	r	NEXT-0.6m	28653
103.2	17.86	0.1	0.1	i'	NUTTelA-TAO/BSTI	28674
103.2	18.16	0.1	0.1	r'	NUTTelA-TAO/BSTI	28674
157.6	16.96	0.1	0.1	i'	NUTTelA-TAO/BSTI	28674
157.6	17.91	0.15	0.15	g'	NUTTelA-TAO/BSTI	28674
157.6	16.81	0.1	0.1	r'	NUTTelA-TAO/BSTI	28674
202.6	16.75	0.1	0.1	i'	NUTTelA-TAO/BSTI	28674
202.6	17.76	0.15	0.15	g'	NUTTelA-TAO/ BSTI	28674

This paper has been typeset from a TEX/LATEX file prepared by the author.